International Journal of Applied Earth Observations and Geoinformation 111 (2022) 102841

Contents lists available at ScienceDirect

International Journal of Applied Earth Observations and Geoinformation

journal homepage: www.elsevier.com/locate/jag

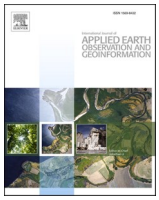

Refinement of semantic 3D building models by reconstructing underpasses from MLS point clouds

Olaf Wysocki *, Ludwig Hoegner, Uwe Stilla

Photogrammetry and Remote Sensing, TUM School of Engineering and Design Technical University of Munich, Arcisstr. 21, 80333 Munich, Germany

ARTICLE INFO

Keywords:
MLS point clouds
Building reconstruction
Semantic 3D building models
Underpasses
Buildings refinement
Bayesian networks
Uncertainty

ABSTRACT

Semantic 3D building models are provided by public authorities and can be used in applications, such as urban planning, simulations, navigation, and many others. Since large-scale 3D models are typically derived from top-view digital surface models (DSM), they can have detailed roof structures but render planes for façade elements. Furthermore, buildings' underpasses are often unmodeled, which impacts road space modeling and the building's volume score. For refining semantic 3D building models, point clouds obtained from mobile laser scanning (MLS) seem to be suitable. In this paper, we present a method of underpass reconstruction by comparing building models' façades with co-registered MLS measurements. As an alternative approach to from-scratch reconstruction, it exploits existing semantic 3D building models and street-level MLS point clouds to enhance models where required. The method considers the uncertainties of 3D models and measurements in a Bayesian network. Analyzed conflicts between the two representations resulting from ray tracing are used to delineate the underpass's contours on a façade. Generalized contours are extruded to 3D solid geometries and subtracted from a raw 3D building model, while the semantics is mapped to form an updated semantic 3D building model. The experiments show that the method reaches an accuracy of 12 cm while testing on CityGML LoD2 building models and the open point cloud datasets TUM-MLS-2016 and TUM-FAÇADE representing the Technical University of Munich (TUM) city campus. The validation reveals differences between the reconstructed and updated models in both volumes (up to 18%) and surfaces (up to 20%). Such an extension of road corridors can improve 3D map usage for vehicle navigation and urban simulations.

1. Introduction

Building models are an important basis for numerous applications, such as calculating heat demand (Martirano et al., 2022), assessing flood damages (Apel et al., 2009), simulating wind flows (Montazeri and Blocken, 2013), analysing solar irradiation (Willenborg et al., 2018a,b), and testing automated driving functions (Wysocki et al., 2021a; Schwab and Kolbe, 2019), among others (Biljecki et al., 2015).

Semantic 3D building models are frequently reconstructed from 2D footprints and photogrammetric observations, acquired using multi-view stereo (MVS) or airborne laser scanning (ALS) techniques. For example, more than eight million LoD2 building models in Bavaria, Germany, were created based on cadastral 2D building footprints and ALS measurements, supported by geodetic measurements and aerial-based digital surface models (Aringer and Roschlaub, 2014; Roschlaub and Batscheider, 2016).

However, such LoD2 building models do not display any façade details, as can be seen in Fig. 1b. By comparing the red ellipse in the oblique image (Fig. 1a) with that in the 3D building model (Fig. 1b), we can observe that an underpass is absent in the 3D building model; this issue also occurs in other city models (Wysocki, 2022b). Since an underpass (Fig. 2) *is a part of a building at a ground level intended for vehicles to drive through. It is bounded by walls and a roof* (Special Interest Group 3D, 2020), its modeling seems essential for urban simulations and car navigation applications.

Vehicle-mounted laser scanners, referred to as MLS, can capture dense, street-level point clouds that enable the mapping of road spaces and façade elements such as windows, doors, and underpasses (Xu and Stilla, 2021).

As an alternative to from-scratch reconstruction and point cloud segmentation, we propose a 3D building refinement method that utilizes existing semantic 3D building models and MLS point clouds. To this end, we list our contributions as follows:

* Corresponding author.
E-mail addresses: olaf.wysocki@tum.de (O. Wysocki), ludwig.hoegner@tum.de (L. Hoegner), stilla@tum.de (U. Stilla).

https://doi.org/10.1016/j.jag.2022.102841
Received 23 February 2022; Received in revised form 19 May 2022; Accepted 24 May 2022
Available online 8 June 2022

(a)

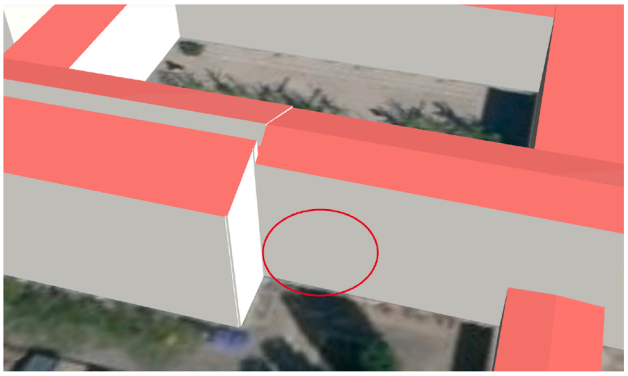

(b)

Fig. 1. Comparison of an oblique image and a 3D city model, both with a red-circled underpass, in Munich, Germany. a) Oblique image (Google Earth, 2022), b) 3D building models at level of detail (LoD)2 (BayernAtlas, 2022).

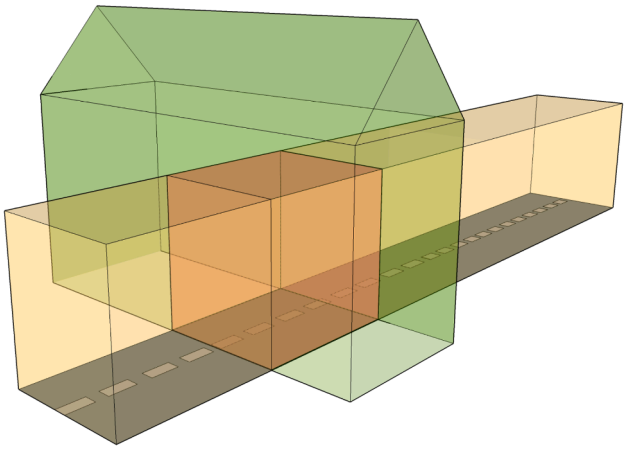

Fig. 2. Visualization of the presented underpass definition.

- A method of refining existing semantic 3D building models with reconstructed underpasses using MLS point clouds with a published code (Wysocki, 2022a).
- An approach that addresses multimodal uncertainties of MLS point clouds, semantic 3D building models, and 2D vector road features.
- A seamless comparison between multimodal datasets that considers different states of voxels in conjunction with a building model.
- A CityGML-compliant method of underpass modeling, according to the definition by Gröger et al. (2012),Special Interest Group 3D (2020) and visualized in Fig. 2.

2. Related work

Comparisons between newly acquired and existing data generally involve detecting changes over time. In this work, we distinguish between changes detected in unimodal (i.e., point cloud to point cloud) and multimodal (i.e., point cloud to vector) datasets; related to multimodal conflicts independent of time.

2.1. Change detection between point clouds

A method of detecting changes in different terrestrial laser scanning (TLS) point clouds is presented by Zeibak and Filin (2008). To perform a point-wise comparison, they transform each scan into image panoramas. They define three possible states between point cloud epochs, such as *change*, *no change*, and *occlusion*.

Hebel et al. (2013) introduce a voxel grid for change detection. The uncertainty is modeled using Dempster–Shafer theory (DST). Based on ray tracing, they distinguish between three states: *occupied*, *empty*, and *unknown*, subsequently deriving the states: *consistent*, *disappeared*, and *appeared*. Hirt et al. (2021) pursue this idea using MLS point clouds to identify changes of urban trees.

The works by Hebel et al. (2013) and Hirt et al. (2021) differ in the role of the voxel grid and the choice of the voxel size. While Hebel et al. (2013) choose a coarse voxel size to accelerate the search for conflicts and to conduct post-processing to identify changes, Hirt et al. (2021) employ a fine voxel size to directly determine conflicts and changes.

In the work by Gehrung et al. (2017) a Bayesian approach is favored for a fusion of MLS single sensor measurements. They present a method of removing dynamic objects in scenes by accumulating probabilities of voxel occupancy, which decrease when the voxel is traversed by a laser ray. The work is incorporated in the probabilistic *OctoMap* framework (Hornung et al., 2013) using an efficient octree structure for calculations.

2.2. Multimodal change detection

Tuttas et al. (2015) propose a probability-based method of progress monitoring in construction sites to compare an as-planned state derived from a building information modeling (BIM) model to an as-built state represented by a photogrammetric point cloud. They also elaborate on the challenges they encountered in such multimodal comparisons.

However, BIM models are distinct from semantic 3D city models, especially concerning the geometrical representation; while BIM components are typically generated using volumetric geometries, semantic 3D city models are frequently represented by outer-observable surfaces (Kolbe and Donaubauer, 2021).

In our previous work (Wysocki et al., 2021b), we explore Bayesian network (BayNet) possibilities and introduce confidence interval (CI) for fusion of MLS point clouds and semantic 3D city models. We focus on a combination of both to identify possible façade surface enhancements while considering uncertainties. Yet, we approach the issue without information on MLS sensor origin, which limits possibilities of comprehensive change detection for features such as windows, doors, or underpasses, among others.

2.3. Refinement of 3D building models

Substantial research effort has been devoted to detecting and reconstructing façade elements (Musialski et al., 2013). Methods typically focus on such façade elements as windows (Tuttas and Stilla, 2013; Aijazi, 2014; Becker, 2011; Iwaszczuk et al., 2011), windows and doors (Ripperda, 2010; Riemenschneider et al., 2012), balconies (Fan et al., 2021), and general surface details (Wysocki et al., 2021a). To the best of our knowledge, no research to date has considered refining buildings with underpasses, although they significantly impact the representation of façades and road spaces.

Work relating to underpasses has been undertaken by Gargoum et al. (2018), where they assess the vertical clearance of overhead assets such as bridges. Their solution is based on light detection and ranging (LiDAR) point clouds acquired in MLS campaigns on highways. The method first detects overhang objects as possible candidates and classifies them into either bridge or non-bridge structures. The selection is based on the assumptions that a point measured above a vehicle trajectory suggests an existing overhang asset; a bridge represents a denser region than a non-bridge asset. Testing was performed on three highways with a total of 38 bridges and 124 other vertical assets. The method was successful in classifying overhead structures into bridges and non-bridges, with an accuracy level of approximately 96%.

In the method of González-Jorge et al. (2013) a bridge structure detection is proposed. They employ automatic segmentation of road overpasses to detect mortar efflorescence.

Tunnel structures are addressed in the work by Puente et al. (2016), which presents a solution for inspecting a vertical clearance space along tunnels. The assumption is made that no global navigation satellite system (GNSS) signal is available and relative orientation to road lanes has to be established.

Despite the similarities, an underpass is a part of a building that distinguishes it from alike structures, such as bridges or tunnels; these are perceived as single entities within the road space, whereas the underpass is indissolubly linked to a building within the road space.

An alternative identification method is proposed by Dukai et al. (2020), where a topology of a cadastral vector map is used to detect multi-level buildings. Such a map-based approach of underpasses identification can be also pursued by conversion of BIM models to semantic city model formats Kolbe and Donaubauer (2021).

In the BIM context, too, reconstruction of objects without a solidification process has been undertaken (Krijnen and Beetz, 2017). However, semantic point cloud embedding in the large-scale city models is currently limited (Beil et al., 2021).

3. Proposed methods

In contrast to the previous work that examines façade surface refinement (Wysocki et al., 2021b; Wysocki et al., 2021a), this paper focuses on refining semantic 3D building models with underpasses detected using MLS point clouds.

The workflow (Fig. 3) starts with an evaluation of input dataset uncertainties (Section 3.1). A ray casting process identifies states (labels) for voxels of MLS point clouds (Section 3.2). The 3D model's faces are compared with labels of the voxels to identify changes between existing building models and new MLS measurements. If conflicts are found between the 3D model and labeled voxels (Section 3.3), the process continues to *Probabilistic classification*; otherwise, it selects another 3D building model from a database. The *Probabilistic classification* step classifies the detected conflicts (Section 3.5). Collateral information is derived from vector road features (Section 3.4) to detect underpasses. If an underpass feature is found, a shape extraction step is performed (Section 3.6.1), followed by a contour generalization step (Section 3.6.2); otherwise, another respective *module* is started. The underpass's contours are used to extrude an underpass to a 3D entity, which is subtracted from the solid geometry of an input 3D building (Section 3.6.3). This process generates a refined 3D building solid geometry. Ultimately, the unchanged and the updated semantics of the 3D building model are assigned to the respective parts of the geometry (Section 3.6.4).

3.1. Datasets with inherited uncertainties

Addressing uncertainties is especially challenging when concerning multimodal datasets. Vector objects and laser measurements have various uncertainties, which can stem from acquisition techniques, data processing, or imprecisely described metadata, among others. For example, horizontal features have different uncertainties from vertical ones.

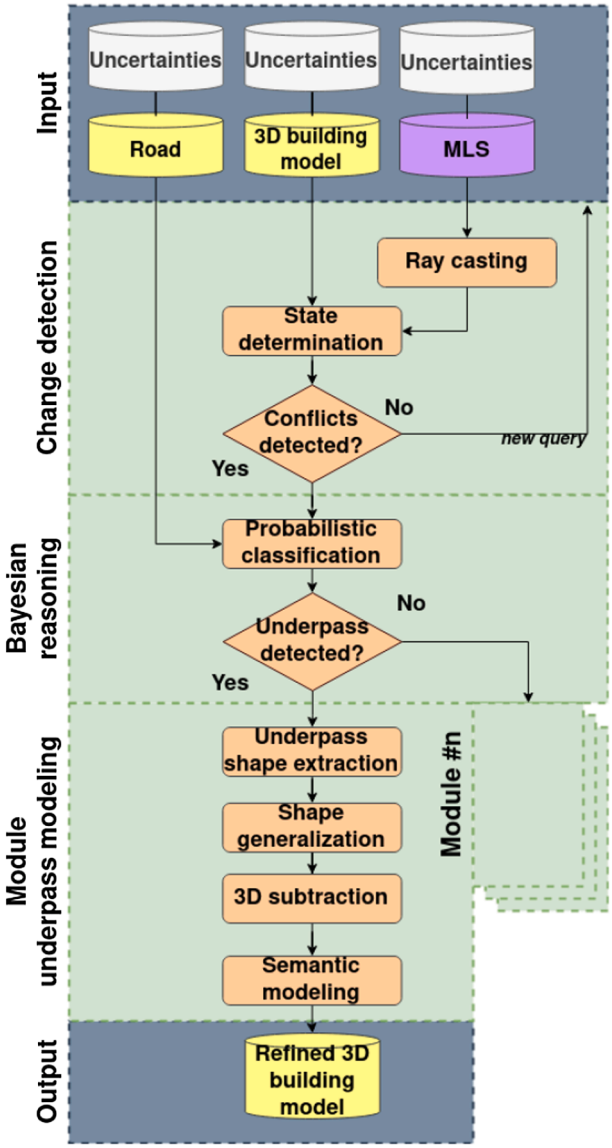

Fig. 3. Overview of the presented workflow.

The proposed uncertainty assignment method investigates two 3D spatial object classes, namely façades and roads, each of which is addressed differently. The addressing of façades concerns the global positioning accuracy of point clouds and building models, while for roads it is the uncertainty of location, buffering, and 3D extrusion of vector road features. Confidence intervals (CI) are introduced to quantify these multimodal uncertainties. The CI is estimated based on the confidence level (CL), with its associated z value (z), standard deviation (σ), and mean (μ).

The CI for façades is estimated using $\sigma = \sqrt{\sigma_1^2 + \sigma_2^2}$. Assuming Gaussian distribution and operating in the L1 norm, the maximum upper and lower bounds are given by $[\mu_i - 2\sigma_i, \mu_i + 2\sigma_i]$ (Suveg and Vosselman, 2000). σ_1 describes the location uncertainty of MLS point clouds, while σ_2 addresses the uncertainty of semantic 3D building walls. The assumptions are made for the point cloud global registration error e_1 and for the global location error of building model walls e_2. The operator's belief regarding the deviation from the true value is quantified using the confidence levels CL_1 and CL_2 for point clouds and building model walls, respectively. Both confidence levels CL_i are bound to the respective z_i

value, while μ_i divided by z_i is an estimate of the standard deviation σ_i value (Hazra, 2017).

The CI for roads can be derived from numerous studies of 2D vector road map uncertainties (Neis et al., 2012; Haklay, 2010; Minghini et al., 2018). Based on derived standard deviations and identified beliefs, a road's linear position in 2D is quantified using the same formulas as for façades. Width buffering and height extrusion are then performed on the basis of road span norms (Fiutak et al., 2018; FGSV, 1996; Chacon, 2020) and clearance space norms (Chacon, 2020; U.S. Department of Transportation, 2014; Holst and Holst, 2004).

3.2. Ray casting

Automatic visibility analysis is conducted to identify missing semantic model elements. An occupancy grid is introduced to analyze the multimodal data of the semantic 3D building models and the MLS observations. The grid is an octree structure encompassing a volume of interest, in which 3D voxels are the octree's leaves. The 3D voxels are used to search for conflicts between the semantic 3D building models and the MLS measurements, where the voxels' size v_s is chosen according to the expected uncertainties of the 3D building model and the MLS point cloud.

A measurement by the laser scanner is emitted from the position of the sensor s_i, oriented by the vector r_i, and pointing toward the reflective position $p_i = s_i + r_i$ (Fig. 4). These variables can be extracted from the MLS set up (Zhu et al., 2020). Voxels that cover p_i are labeled as *occupied* (blue), those between s_i and r_i as *empty* (pink), and those behind p_i and traversed by the elongated ray as *unknown* (gray).

Repeated voxels' observations are considered in a probabilistic fashion, as shown by Moravec and Elfes (1985). Probabilities are assigned using log-odds notation and clamping policy, following the concept of Hornung et al. (2013), Tuttas et al. (2015). The values of l_{min} and l_{max} are used to define the clamping thresholds of the log odd-values $L(n)$:

$$L(n|z_{1:i}) = max(min(L(n|z_{1:i-1}) + L(n|z_i), l_{max}), l_{min}) \tag{1}$$

where

$$L(n) = log[\frac{P_n}{1 - P(n)}] \tag{2}$$

Faces are inserted into the occupancy grid (brown in Fig. 4)) to enable a comparison between the point cloud and vector model. Each inserted face has an uncertainty given by the estimated upper bound of the CI and the associated CL. The upper CI defines a range of façade position deviations, while the CL indicates its associated belief. Finally, each voxel is represented by the position, size, and probabilities relating to the model and measurements.

3.3. Comparison of point cloud to building model

The façades are subjected to a piece-wise comparison by analyzing the state of the voxels (Fig. 5): Voxels determined by laser observations as having the state *occupied* and that are occupied by the intersection of façades are labeled as *confirmed* (green); while voxels labeled as *empty* by the laser observations and which intersect with façades are labeled as *conflicted* (red).

A texture map is defined for each façade of the building model. It has a cell spacing c_s, following the projection of the voxel grid to the plane. Each pixel in the texture map is labeled in relation to the voxel's state as *confirmed* or *conflicted*. Consequently, the areas of the façade uncovered by the MLS observations are labeled as *unknown* (grey).

The next processing step depends on the ratio $r_c \in [0, 1]$ of the number of pixels with the state *conflicted* a_1 to the total surface area of façade a_2, including *unknown* and *confirmed* parts.

$$r_c = \frac{a_1}{a_2} \tag{3}$$

If r_c is smaller than $r_{c_{min}}$, we deem the modeled façade to be correct, which means that any refinement is superfluous. If r_c is greater than $r_{c_{max}}$, we assume that the modeled façade is significantly erroneous and a refinement is unviable. The modeled façade is therefore only considered

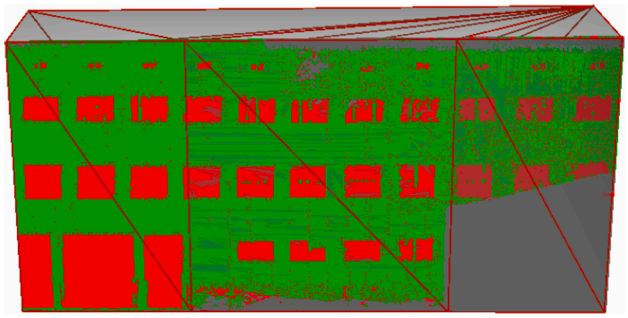

Fig. 5. Example of a texture map showing the states *confirmed*, *conflicted*, and *unknown*, for the building shown in Fig. 1.

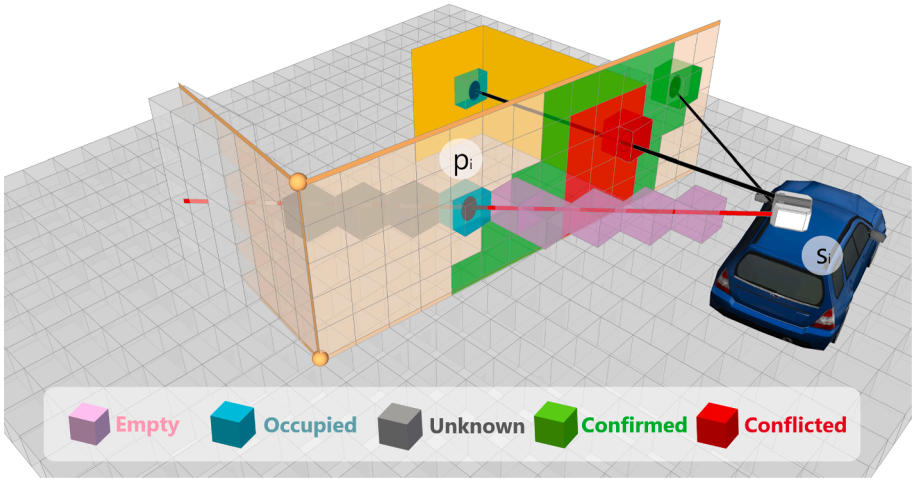

Fig. 4. Ray casting on a 3D octree grid from the sensor position s_i to the reflection point p_i: The voxels encompassing the p_i points are deemed as *occupied* (blue), traversed voxels as *empty* (pink), and others as *unknown* (grey). The voxels are *confirmed* (green) when the façade's face intersects with *occupied* voxels and are *conflicted* if the façade's face intersects with *empty* voxels.

for the refinement when its ratio r_c is: $r_c \in [r_{c_{min}}, r_{c_{max}}]$

3.4. Comparison of map to building model

Underpasses are classified considering the state of the texture map, state uncertainties, and additional road information. Since the road data are assumed to represent 2D lines, they are 2D-buffered and then vertically extruded to the probable 3D clearance space using CI, as discussed in Section 3.1. Such 3D vector volume is intersected with the façade in question. The intersection area displays *map conflict* on the second layer of the texture map (shown in purple in Fig. 6).

3.5. Probabilistic classification: the Bayesian approach

Underpasses are classified using input textures in BayNet (Fig. 6). Our BayNet comprises of one target (red) and two input nodes (yellow). The causal relationship between the *X* and the *Y* nodes is expressed by directed links. Each node is a variable with two categorical, mutually-exclusive states. The target state is calculated based on the joint probability distribution $P(X, Y)$ and the conditional probability table (CPT), which prescribe the probabilities of each node and each combination of parent node states. The probability that the node *Y* (*Underpass space*) is in the state *y* (*underpass*) is estimated using the so-called marginalization process (Stritih et al., 2020), which sums conditional probabilities of the states *x* (i.e., *map conflict*, *confirmed*, *conflicted*, or *unknown*) belonging to the parent nodes *X* (i.e., *Map comparison* and *Point cloud comparison*).

When the network is compiled, datasets are added as evidence for updating the joint probability distribution. In our case, it is soft evidence as the datasets comprise texture layers with inherited uncertainties, due to the CI measure. The update is performed by an inference process, which estimates the posterior probability distribution (PPD) yielding the most likely node states (Stritih et al., 2020).

It is assumed that the co-occurrence of the pixel states *conflicted* and *map conflict* leads to a high probability estimation for underpasses. The decision node (blue in Fig. 6) steers the procedure based on the probability score *P* of each pixel in the resulting texture: If any pixel score *P* is greater than P_{high}, then an *Unmodeled underpass* is present within a texture and should be modeled; pixels with a P_{low} score represent *Other objects*. An example of such a probability texture is given in Fig. 7, where

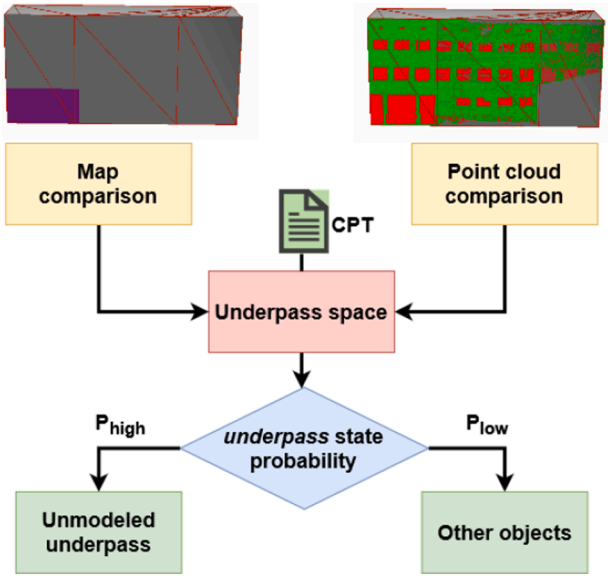

Fig. 6. The designed BayNet: Input nodes (yellow) estimate the underpass space probability (red) quantified by CPT resulting in the decision node (blue), which determines whether a façade has any unmodeled underpasses or if conflicts are caused by other objects (green).

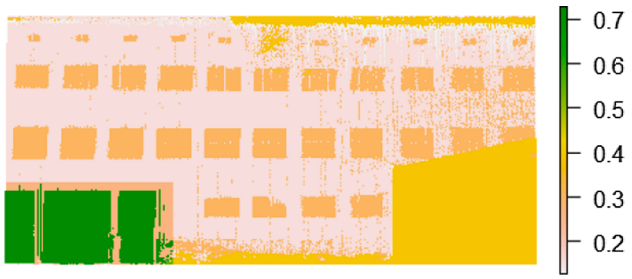

Fig. 7. Probability texture: BayNet estimates the probability for each pixel for the target node state *underpass*.

green pixels represent a P_{high} score for unmodeled underpasses, while the other pixels represent a P_{low} score for other objects.

3.6. Modeling of underpasses

Section 3.6.1 shows the underpass modeling process, in which a detected underpass space is first delineated by vector polygons on a façade. Section 3.6.2 then describes how to minimize the noise impacting the underpass's shape. The generalized shape is used to create a 3D representation of the underpass space. An underpass in a building is modeled using the constructive solid geometry (CSG) difference operation, in which the reconstructed space is subtracted from a raw 3D building geometry, as shown in Section 3.6.3. The final step, presented in Section 3.6.4, shows semantic modeling in a CityGML-compliant way.

3.6.1. Extracting shape of underpasses

The shape of an underpass is extracted using the probability texture, discussed in Section 3.5 and shown in Fig. 7. The P_{high} threshold is used to segment pixels depicting the underpass's shape: If the *P* score is greater than P_{high}, the pixels are regarded as underpass candidates; otherwise, they are rejected. The candidates are clustered if they have a neighbor in any of the eight directions of a pixel. This process merges single, adjacent pixels into clusters, now serving as blobs.

In this stage, noisy blobs are rejected if they are smaller than or equal to the chosen area threshold value b_s. Any blobs larger than threshold b_s constitute the underpass shape candidates. At the end of the process, the contour of each blob is transformed into a vector polygon. An example of extracted shapes is illustrated in Fig. 8a.

3.6.2. Generalizing shape of underpasses

As shown in Fig. 8a, the contour lines of the extracted blobs can display noise, spikes, and inclusions. The generalization process removes inclusive polygons on the basis of topological relations. It then approximates the outer shapes using the modified Douglas-Peucker algorithm, which considers parameters related to distances d_1, d_2, and angles a_1 (Douglas and Peucker, 1973). Any blobs that are not connected to the ground, are extended toward the ground surface to overcome the so-called border effect, visible in Fig. 8a. The final, generalized shapes are shown in Fig. 8b.

3.6.3. Reconstructing underpasses using CSG

A 3D underpass is reconstructed based on the generalized shapes that are extruded in a perpendicular direction and at the length measured from the investigated façade to the corresponding back-façade. This leads to the formation of prismatic objects (Fig. 9), which represent the input solids for a CSG tree (Fig. 10). It should be noted that the prismatic objects do not represent tangible objects but rather a free space. They are therefore first aggregated (∪) and then subtracted (–) from a solid building geometry, as shown in Fig. 10 (Wyvill and Kunii, 1985). The subtraction remodels intersected polygons and closes inner-building gaps using face-intersecting vertices of the underpass space, thereby partitioning the polygons into smaller parts and closing gaps with

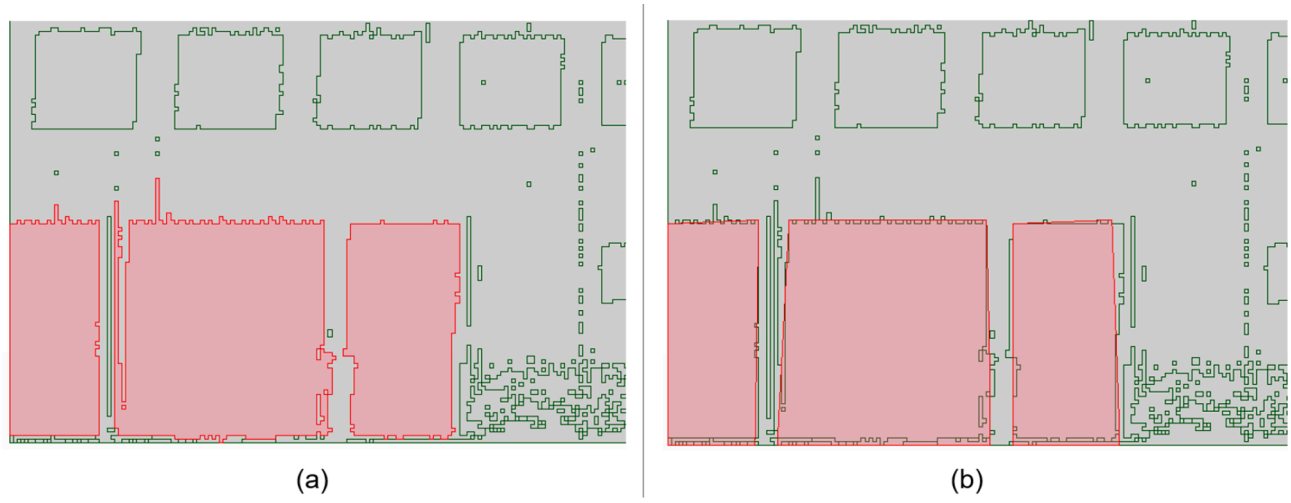

Fig. 8. Shape extraction process. a) Identified underpass blobs, b) generalization of extracted shapes.

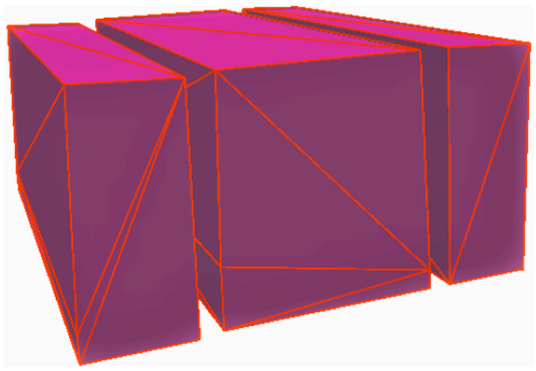

Fig. 9. Prismatic 3D volumes of an underpass.

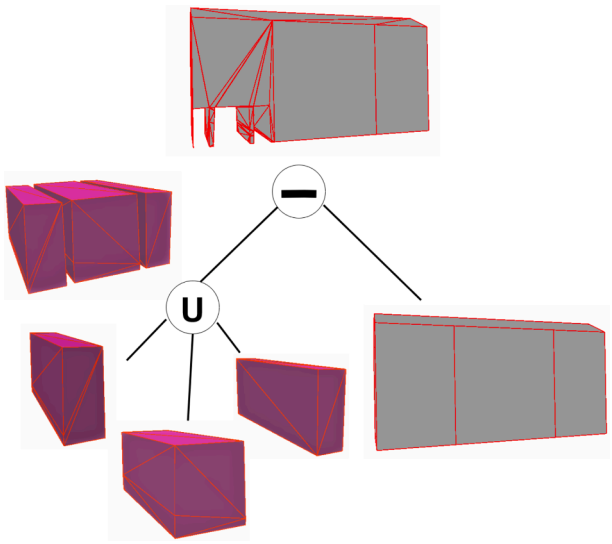

Fig. 10. CSG tree: Union of the underpass volumes (∪) and its difference (–) to the solid volume of the building results in a refined building model.

polygon triangles.

3.6.4. Modeling of 3D semantics

By this stage of the workflow, the geometry of the building in question is refined, as illustrated in Fig. 12. Now, the task is to embed the refined geometric and semantic information in the refined 3D model. First, new inner walls and ceiling surfaces obtain a unique identifier (ID) and are defined as constituents of the single underpass entity, which obtains a unique ID, too. Since the underpass semantically belongs to the *BuildingInstallation* class and as such links by a parent ID to the solid building entity, it is modeled accordingly following Special Interest Group 3D (2020). Furthermore, the reserved for underpasses function *1002* of the *BuildingInstallation* class in the CityGML standard (Special Interest Group 3D, 2020) is assigned to the underpass entity. Note that although it is possible to model the underpass at LoD2, we opt for its representation at LoD3 (LoD3.2). This is due to the fact that we identify the underpass as a large (i.e., exceeding 1 m^2) façade opening (Gröger et al., 2012; Biljecki et al., 2016; Special Interest Group 3D, 2020).

Moreover, generic attributes are created that extend the plain description of added geometries, namely, *maxClearance* and *refinementDate*. The semantic enrichment is illustrated in Fig. 11, where red edges mark the underpass entity, and the respective semantic is visualized in the attribute table.

4. Experiments and results

4.1. Datasets for the TUM Campus test site

We selected the TUM Main Campus in Munich, Germany, as a test area and acquired CityGML LoD2 building models, OpenStreetMap (OSM) roads, and MLS point clouds, as shown in Fig. 13.

The CityGML LoD2 building models represented governmental data created on a basis of cadastre and aerial measurements (Roschlaub and Batscheider, 2016; Aringer and Roschlaub, 2014). The building models

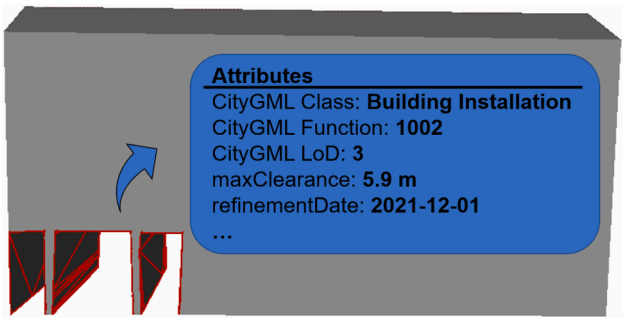

Fig. 11. The semantically modeled underpass structure as a *BuildingInstallation* with the respective CityGML function: *1002*.

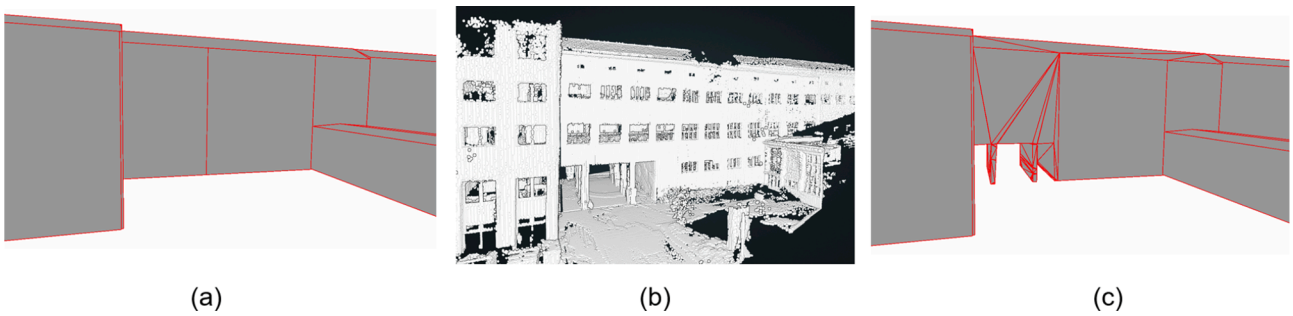

Fig. 12. Semantic 3D building model refined by the addition of an underpass using MLS point clouds. a) Raw city model, b) point cloud, c) refined building model.

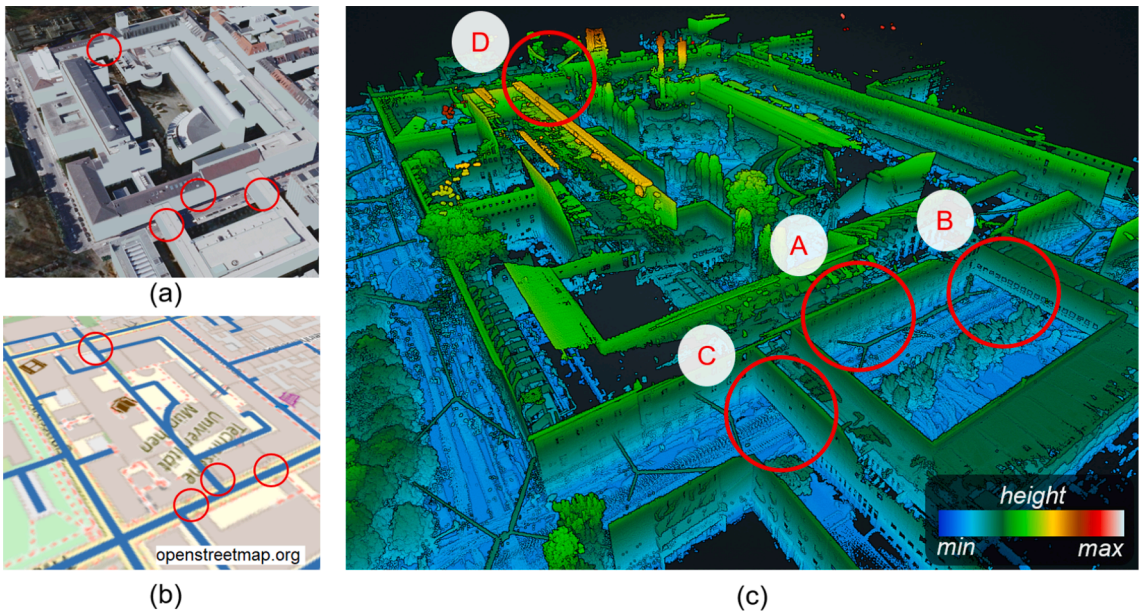

Fig. 13. The TUM Campus dataset and selected underpasses (red). a) CityGML LoD2 building models (TUM Geoinformatics, 2022), b) OSM roads (OpenStreetMap contributors, 2021), c) MLS point clouds (Zhu et al., 2020).

are shown in Fig. 13a, taken from the 3DCityDB-Web-Map-Client service (TUM Geoinformatics, 2022).

The OSM road features were acquired from Geofabrik resources (Geofabrik, 2020). Thoroughfares unsuitable for driving were subsequently rejected by discarding the classes: footway, pedestrian, bridleway, cycleway, path, steps, and unknown (Ramm, 2021). Driveable roads (blue) are shown in Fig. 13b.

The MLS point clouds were extracted from the open TUM-MLS-2016 dataset (Fig. 13c) introduced by Zhu et al. (2020). We used the raw point clouds with sensor positions transformed to the global coordinate reference system (CRS). Additionally, we used TUM-FAÇADE's annotated point clouds (Wysocki et al., 2021c) and enriched them for validation with manually labeled point clouds representing underpasses.

4.2. Parameter settings for uncertainties

The uncertainty of a façade's global position was incorporated using input parameters for MLS point clouds and CityGML models. For the MLS point cloud global registration error we set $e_1 = 0.3$ m, $\mu = 0.15$ m, $CL_1 = 90\%$, and $z_1 = 1.64$, while for CityGML building model global positioning accuracy error we set $e_2 = 0.03$ m, $\mu = 0.015$ m, $CL_2 = 90\%$, and $z_1 = 1.64$. This resulted in an estimate for the façades' upper CI of 0.2 m.

Based on the studies by Haklay (2010), we set the location error for roads to $e_3 = 5.83$ m, at $CL_3 = 75\%$, and $z_3 = 1.15$. The 2D upper CI of the roads were multiplied by a factor that varied depending on the road type: 1.5 for a service road and 6 for a secondary road, following the 3D-DLM project (Fiutak et al., 2018). This resulted in 2D buffers equaling 6.6 m and 11.1 m for service and secondary roads, respectively. The roads were then vertically extruded based on a top minimum clearance space height study (Chacon, 2020) and estimated at 6.5 m. Extrusion was performed for roads intersecting with a CityGML building model or that had an overlapping OSM feature indicated by a value *T* for the attribute *tunnel* (Ramm, 2021).

4.3. Parameter settings for ray casting

We used an octree voxel grid with the leaf size set to $v_s = 0.1$ m, to find fine deviations and simultaneously suppress noise. Each voxel was initialized with a uniform prior probability of $P = 0.5$. Following Hornung et al. (2013) and Tuttas et al. (2015), we decided to use log-odds values of $l_{occ} = 0.85$ for *occupied* and $l_{emp} = -0.4$ for *empty*, corresponding to $P_{occ} = 0.7$ and $P_{emp} = 0.4$, respectively. Each untraversed space was labeled as *unknown*. The clamping thresholds were set to $l_{min} = -2$ and $l_{max} = 3.5$, corresponding to $P_{min} = 0.12$ and $P_{max} = 0.97$, respectively.

We assessed the plausible CI for a 3D building model face, which scored 0.2 m with $CL = 90\%$, as discussed in Section 4.2.

4.4. Parameter settings for point cloud to model comparison

For each façade, a texture layer was created with rows and columns corresponding to the rows and columns projected to the façade's face. Using the analysis presented in Section 3.3, we identified and projected to the texture three states: *conflicted*, *confirmed*, and *unknown*.

We then set the threshold ratio of $r_{c_{min}} = 0.1$ and $r_{c_{max}} = 0.6$ between the conflicted pixels area a_1 and the total surface area a_2. In most cases, however, the façades qualified to the classification step, as the ratio r_c was within the permitted interval of conflict areas per face, where $r_c \in [0.1, 0.6]$.

4.5. Detection and classification of underpasses

The designed BayNet requires two inputs: the point cloud comparison layer (Section 3.3) and the map comparison layer (Section 3.4). Therefore, the inputs comprised two items of soft evidence with geometrical representations and inherited beliefs. According to the estimated CI, the input beliefs resulted in 75% and 90% evidence for the map comparison layer and the point cloud comparison layer, respectively. The probability threshold defining *Unmodeled underpass* and *Other objects* was set to $P_{high} > 0.7 >= P_{low}$.

All four underpasses indicated in Fig. 13 were correctly identified. Reconstructed underpasses are shown for building A in Fig. 12 and for buildings B, C, D in Fig. 14.

4.6. Extracting shape of underpasses

We defined the threshold as $b_s = 1.5\ \mathrm{m}^2$ to suppress irrelevant blobs. The shapes were then generalized by a modified Douglas-Peucker algorithm with the parameters set to $d_1 = 0.1, d_2 = 0.3$, and $a_1 = 45°$.

4.7. Validation of underpass refinement

The validation was conducted using the ground-truth point clouds, which represented the underpasses, while volume and surface changes were compared using refined building models (LoD3) and raw building models (LoD2). The results of the validation are shown in Table 1 and Fig. 15, while Table 2 and Table 3 present surface and volume changes, respectively.

The most remarkable result to emerge from the experiments was that deviations in automatically modeled underpasses ranged from 1 cm to 23 cm and had a mean mode score of 12 cm, as shown in Table 1. As hypothesized, the experiments showed that underpasses contribute significantly to a building's envelope surface; the mean score for the surface difference was 13%, reaching up to 20%. Note that the score for underpass B was 4% since the building model is vast and thus has a large

Table 1
Validation of automatically modeled underpasses compared to the ground truth point clouds.

Building	*Median* [m]	*Mode* [m]	*RMS* [m]
A	0.18	0.01	0.29
B	0.19	0.07	0.38
C	0.25	0.06	0.52
D	0.28	0.23	0.45
μ	**0.22**	**0.12**	**0.41**

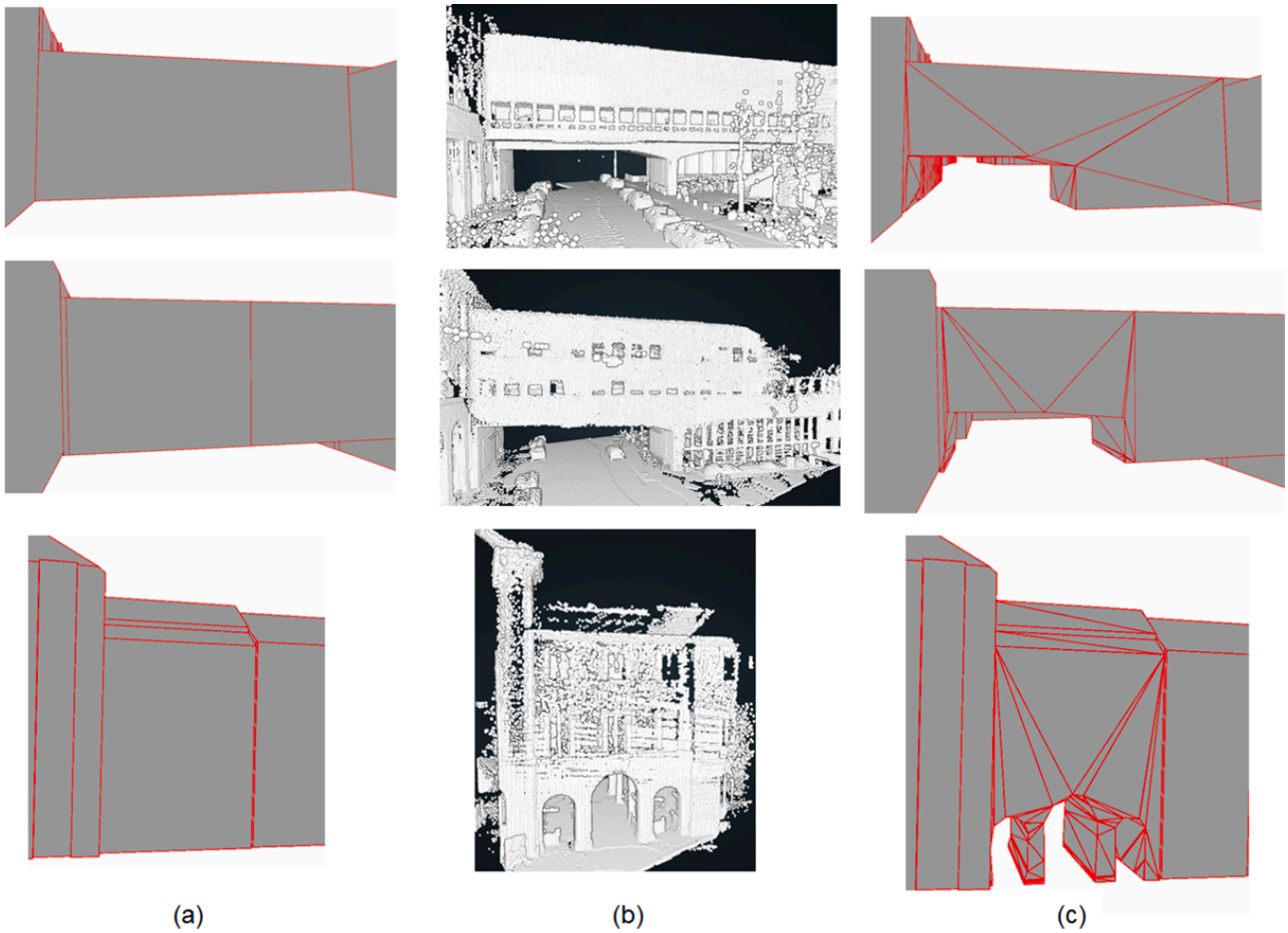

Fig. 14. Refinement results for the buildings B, C, and D. a) Raw city model, b) point cloud, c) refined city model.

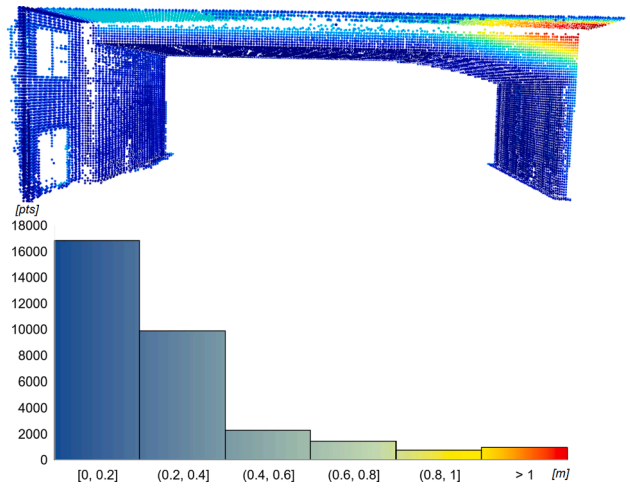

Fig. 15. Histogram and visualization of projected Hausdorff distances to a ground-truth point cloud for underpass B, given in meters.

Table 2
Surface refinements for refined models (LoD3) compared to raw (LoD2) building walls and ground surfaces.

Building	Surf. LoD2 [m^2]	Surf. LoD3 [m^2]	Diff. [m^2]	Diff. [%]
A	2,724	2,448	276	10
B	10,132	9,716	416	4
C	1,918	1,534	384	20
D	1,058	874	184	17
μ			**315**	**13**

Table 3
Volume refinements for refined models (LoD3) compared to raw building models (LoD2).

Building	Vol. LoD2 [m^3]	Vol. LoD3 [m^3]	Diff. [m^3]	Diff. [%]
A	11,994	11,116	878	7
B	70,110	68,962	1,148	2
C	6,434	5,403	1,031	16
D	2,898	2,380	518	18
μ			**894**	**11**

surface area. We present all surface-related comparisons in Table 2. The mean score for volume deduction was 11%, reaching up to 18%, as shown in Table 3.

5. Discussion

The experiments demonstrated promising results for the method of refining 3D building models by underpasses, after successfully applying to four underpasses in the TUM campus area.

There are two possible reasons for the deviations shown in Table 1: Underpasses' shapes are generalized and inevitably indicate a degree of deviation (e.g., building D in Fig. 14); underpasses' shapes are horizontally extruded to form prismatic 3D entities and as such neglect inner-space discontinuities (e.g., the step-like ceiling in building B shown in Fig. 14b and in Fig. 15).

Experiments incorporating the CI are in accordance with OSM and vertical clearance space studies. The set of parameters chosen to transform 2D road features to 3D spaces represents a satisfactory agreement between the under- and over-estimation of underpass shapes.

In the ray casting process (Section 3.2), we elaborate on an appropriate 3D voxel size v_s. Here, for the underpasses reconstruction, we select 0.1 m as the appropriate value. For this voxel size, the co-registration accuracy of the MLS point clouds and the semantic 3D city models must be in the cm domain. Deviations in co-registration can lead to the effect that façades cannot be correctly confirmed with this method.

It is worth mentioning that our solution of semantic modeling is based on the CityGML standard (Gröger et al., 2012). However, the method can be seamlessly adjusted to other 3D building model standards and be applied in various encodings, for example CityJSON (Ledoux et al., 2019).

Furthermore, we use the standard CityGML 2.0 data model for assigning semantics of underpasses. For incorporating further details, this approach could be enhanced in future work by developing an application domain extension (ADE), which customizes capabilities of the default CityGML data model to a specific scenario (Gröger et al., 2012; Biljecki et al., 2021).

6. Conclusion

Our work has led us to the conclusion that the refinement of existing models, instead of from-scratch reconstruction, is a promising strategy; it minimizes possible planarity issues and maintains the consistency of city models while reducing the complexity of reconstruction by focusing solely on the model's required changes.

The current refinement method pursues a data-driven strategy. As an alternative, a model-driven approach could use predefined libraries of underpasses and parameters to fit the geometries into classified point clouds.

The validation shows that the achievable accuracy lies within a range of 1 cm to 23 cm. This accuracy can be acceptable when refining models in high definition (HD) maps used for autonomous driving purposes (Wong et al., 2020), extended solar potential analyses based on façades (Willenborg et al., 2018a), or energy demand estimations (Martirano et al., 2022), among other applications (Biljecki et al., 2015). However, the achieved accuracy could limit the method's usability in cultural heritage preservation applications (Grilli and Remondino, 2019).

Evidence from this study suggests that the method may be of particular importance in applications significantly exploiting buildings' surfaces and volumes; surface differences in the context of underpasses may be as high as 20% between an original and a refined building, which can significantly impact estimating solar potential (Willenborg et al., 2018a), analysing urban farming potential (Palliwal et al., 2021), evaluating urban walkability (Zhu et al., 2019) and bikeability (Ito and Biljecki, 2021), and the HD map-based positioning of automated cars (Wong et al., 2020). Furthermore, underpass-related volume differences, reaching up to 18%, can significantly impact energy demand estimations (Martirano et al., 2022).

The proposed, widespread vector data and an unprecedented growth of MLS point clouds stack (Wysocki et al., 2022) promise replicability of the method. Remarkably, even in case of absent 3D building models, they can be generated using OSM footprints, as in the example of Singapore, where underpass-related issues are encountered, too (Palliwal et al., 2021; Wysocki, 2022b). Moreover, the experiments corroborate that the method is applicable for underpasses with a disaggregated profile (i.e., by columns), insignificant discontinuities (i.e., step-like ceilings), and continuous geometry (i.e., elongated profiles). Yet, the method could have limited accuracy for underpasses with inner-vertical intrusions, such as inner domes and inner arches.

Although the four underpasses tested here presented challenging geometries, the small size of the testing sample implies that caution must be exercised. To further our research, we plan to test our solution on a larger number of buildings with underpasses.

Declaration of Competing Interest

The authors declare that they have no known competing financial interests or personal relationships that could have appeared to influence the work reported in this paper.

Acknowledgments

This work was supported by the Bavarian State Ministry for Economic Affairs, Regional Development and Energy within the framework of the IuK Bayern project *MoFa3D - Mobile Erfassung von Fassaden mittels 3D Punktwolken*, Grant No. IUK643/001. Moreover, the work was conducted within the framework of the Leonhard Obermeyer Center at the Technical University of Munich (TUM). We gratefully acknowledge Geoinformatics team at the TUM for valuable insights and for providing the CityGML datasets. OSM map data copyrighted OpenStreetMap contributors and available from https://www.openstreetmap.org.

References

Aijazi, A.K., 2014. 3D urban cartography incorporating recognition and temporal integration. Ph.D. thesis Université Blaise Pascal, Clermont-Ferrand, France.

Apel, H., Aronica, G., Kreibich, H., Thieken, A., 2009. Flood risk analyses–how detailed do we need to be? Nat. hazards 49, 79–98.

Aringer, K., Roschlaub, R., 2014. Bavarian 3D building model and update concept based on LiDAR, image matching and cadastre information. In: Isikdag, U. (Ed.), Innovations in 3D Geo-Information Sciences. Springer International Publishing, Cham, Germany, pp. 143–157.

BayernAtlas, 2022. BayernAtlas, TUM Campus, Theresienstr., Munich, Germany. 3D Buildings data layer. URL: https://geoportal.bayern.de/bayernatlas/?lang=de&topic=ba&bgLayer=atkis&catalogNodes=11&lon=11.56809&lat=48.14691&elevation=842&heading=0.000&pitch=-39.849 (accessed: 2022-01-25).

Becker, S., 2011. Automatische Ableitung und Anwendung von Regeln für die Rekonstruktion von Fassaden aus heterogenen Sensordaten. Ph.D. thesis Universität Stuttgart, Stuttgart, Germany.

Beil, C., Kutzner, T., Schwab, B., Willenborg, B., Gawronski, A., Kolbe, T.H., 2021. Integration of 3d point clouds with semantic 3d city models–providing semantic information beyond classification. ISPRS Ann. Photogramm. Remote Sens. Spatial Inform. Sci. 8, 105–112.

Biljecki, F., Ledoux, H., Stoter, J., 2016. An improved lod specification for 3d building models. Comput. Environ. Urban Syst. 59, 25–37.

Biljecki, F., Lim, J., Crawford, J., Moraru, D., Tauscher, H., Konde, A., Adouane, K., Lawrence, S., Janssen, P., Stouffs, R., 2021. Extending citygml for ifc-sourced 3d city models. Autom. Constr. 121, 103440.

Biljecki, F., Stoter, J., Ledoux, H., Zlatanova, S., Çöltekin, A., 2015. Applications of 3D city models: State of the art review. ISPRS Int. J. Geo-Inform. 4, 2842–2889.

Chacon, M., 2020. Sign guidelines and applications manual. Texas Department of Transportation. URL: http://onlinemanuals.txdot.gov/txdotmanuals/smk/index.htm (accessed: 2021-12-01).

Douglas, D.H., Peucker, T.K., 1973. Algorithms for the reduction of the number of points required to represent a digitized line or its caricature. Cartographica: Int. J. Geogr. Inform. Geovisualiz. 10, 112–122.

Dukai, B., Peters, R., Wu, T., Commandeur, T., Ledoux, H., Baving, T., Post, M., van Altena, V., van Hinsbergh, W., Stoter, J., 2020. Generating, storing, updating and disseminating a countrywide 3d model. Int. Arch. Photogramm. Remote Sens. Spatial Inform. Sci. 44, 27–32.

Fan, H., Wang, Y., Gong, J., 2021. Layout graph model for semantic façade reconstruction using laser point clouds. Geo-spatial Inform. Sci. 24, 403–421.

FGSV, 1996. Richtlinien für die Anlage von Straßen, Teil: Querschnitte, Ausgabe 1996; RAS-Q 96, Forschungsgesellschaft für Straßen- und Verkehrswesen e.V. URL: https://beck-online.beck.de/ (accessed: 2021-11-16).

Fiutak, G., Marx, C., Willkomm, P., Donaubauer, A., 2018. Projekt 3D Digitales Landschaftsmodell (3D-DLM) am Runden Tisch GIS e.V., Abschlussbericht (Demonstrationsphase): Datenvorverarbeitung, Anwendung des 3Dfiers, Abbildung auf CityGML-Datenmodell, Bereitstellung der Ergebnisdaten & Qualitätsbewertung. URL: https://rundertischgis.de/projektarbeit/3d-digitales-landschaftsmodell.html (accessed: 2021-11-11).

Gargoum, S.A., Karsten, L., El-Basyouny, K., Koch, J.C., 2018. Automated assessment of vertical clearance on highways scanned using mobile LiDAR technology. Autom. Constr. 95, 260–274.

Gehrung, J., Hebel, M., Arens, M., Stilla, U., 2017. An approach to extract moving objects from MLS data using a volumetric background representation. ISPRS Annals of the Photogrammetry, Remote Sensing and Spatial. Inf. Sci. IV-1/W1, 107–114.

Geofabrik, 2020. Openstreetmap data extracts. URL: https://download.geofabrik.de/ (accessed: 2020-10-01).

González-Jorge, H., Puente, I., Riveiro, B., Martinez-Sánchez, J., Arias, P., 2013. Automatic segmentation of road overpasses and detection of mortar efflorescence using mobile LiDAR data. Opt. Laser Technol. 54, 353–361.

Google Earth, 2022. Google Earth Pro, TUM Campus, Theresienstr., Munich, Germany. 3D Buildings data layer. URL: http://www.google.com/earth/index.html (accessed: 2022-01-25).

Grilli, E., Remondino, F., 2019. Classification of 3D digital heritage. Remote Sens. 11, 847.

Gröger, G., Kolbe, T. H., Nagel, C., Häfele, K.-H., 2012. OGC City Geography Markup Language CityGML Encoding Standard. Open Geospatial Consortium: Wayland, MA, USA, 2012.

Haklay, M., 2010. How good is volunteered geographical information? A comparative study of OpenStreetMap and Ordnance Survey datasets. Environ. Plann. B: Plan. Des. 37, 682–703.

Hazra, A., 2017. Using the confidence interval confidently. J. Thoracic Dis. 9, 4125.

Hebel, M., Arens, M., Stilla, U., 2013. Change detection in urban areas by object-based analysis and on-the-fly comparison of multi-view als data. ISPRS J. Photogramm. Remote Sens. 86, 52–64.

Hirt, P.-R., Xu, Y., Hoegner, L., Stilla, U., 2021. Change detection of urban trees in MLS point clouds using occupancy grids. PFG J. Photogramm. Remote Sens. Geoinform. Sci. 89, 301–318.

Holst, K.H., Holst, R., 2004. Brücken aus Stahlbeton und Spannbeton: Entwurf, Konstruktion und Berechnung. Ernst & Sohn, Berlin, Germany.

Hornung, A., Wurm, K.M., Bennewitz, M., Stachniss, C., Burgard, W., 2013. OctoMap: An efficient probabilistic 3D mapping framework based on octrees. Autonom. Robots 34, 189–206.

Ito, K., Biljecki, F., 2021. Assessing bikeability with street view imagery and computer vision. Transp. Res. Part C: Emerg. Technol. 132, 103371.

Iwaszczuk, D., Hoegner, L., Stilla, U., 2011. Detection of windows in IR building textures using masked correlation. In: Stilla, U., Rottensteiner, F., Mayer, H., Jutzi, B., Butenuth, M. (Eds.), Photogrammetric Image Analysis, ISPRS Conference - Proceedings, Lect. Notes Comput. Sci., 6952. Springer, Heidelberg, pp. 133–146.

Kolbe, T.H., Donaubauer, A., 2021. Semantic 3D city modeling and BIM. In: Shi, W., Goodchild, M.F., Batty, M., Kwan, M.-P., Zhang, A. (Eds.), Urban Informatics. Springer Singapore, Singapore, pp. 609–636.

Krijnen, T., Beetz, J., 2017. An ifc schema extension and binary serialization format to efficiently integrate point cloud data into building models. Adv. Eng. Inform. 33, 473–490.

Ledoux, H., Arroyo Ohori, K., Kumar, K., Dukai, B., Labetski, A., Vitalis, S., 2019. Cityjson: A compact and easy-to-use encoding of the citygml data model. Open Geospatial Data Softw. Stand. 4, 1–12.

Martirano, G., Pignatelli, F., Vinci, F., Struck, C., Coors, V., Fitzky, M., Hernández, M. G., Serna-González, V., Ramos-Díez, I., Valmaseda, C., 2022. Comparative analysis of different methodologies and datasets for energy performance labelling of buildings. Luxembourg (Luxembourg): Publications Office of the European Union.

Minghini, M., Brovelli, M.A., Frassinelli, F., 2018. An open source approach for the intrinsic assessment of the temporal accuracy, up-to-dateness and lineage of OpenStreetMap. ISPRS Arch. Photogramm. Remote Sens. Spatial Inf. Sci. XLII-4/W8, 147–154.

Montazeri, H., Blocken, B., 2013. CFD simulation of wind-induced pressure coefficients on buildings with and without balconies: Validation and sensitivity analysis. Build. Environ. 60, 137–149.

Moravec, H., Elfes, A., 1985. High resolution maps from wide angle sonar. In: Proceedings of the 1985 IEEE International Conference on Robotics and Automation. St. Louis, MO, USA, vol. 2. IEEE, pp. 116–121.

Musialski, P., Wonka, P., Aliaga, D.G., Wimmer, M., Van Gool, L., Purgathofer, W., 2013. A survey of urban reconstruction. Comput. Graph. Forum 32, 146–177.

Neis, P., Zielstra, D., Zipf, A., 2012. The street network evolution of crowdsourced maps: OpenStreetMap in Germany 2007–2011. Future Internet 4, 1–21.

OpenStreetMap contributors, 2021. Planet dump retrieved from https://planet.osm.org. URL: https://www.openstreetmap.org.

Palliwal, A., Song, S., Tan, H.T.W., Biljecki, F., 2021. 3d city models for urban farming site identification in buildings. Comput. Environ. Urban Syst. 86, 101584.

Puente, I., Akinci, B., González-Jorge, H., Diaz-Vilari no, L., Arias, P., 2016. A semi-automated method for extracting vertical clearance and cross sections in tunnels using mobile LiDAR data. Tunnell. Undergr. Space Technol. 59, 48–54.

Ramm, F., 2021. OpenStreetMap data in layered GIS format: Free shapefiles 2021–07-08. URL: https://download.geofabrik.de/osm-data-in-gis-formats-free.pdf (accessed: 2021-12-01).

Riemenschneider, H., Krispel, U., Thaller, W., Donoser, M., Havemann, S., Fellner, D., Bischof, H., 2012. Irregular lattices for complex shape grammar facade parsing. In: 2012 IEEE Conference on Computer Vision and Pattern Recognition. Providence, RI, USA, CVPR, pp. 1640–1647.

Ripperda, N., 2010. Rekonstruktion von Fassadenstrukturen mittels formaler Grammatiken und Reversible Jump Markov Chain Monte Carlo Sampling. Ph.D. thesis Leibnitz Universität Hannover, Hannover, Germany.

Roschlaub, R., Batscheider, J., 2016. An INSPIRE-konform 3D building model of Bavaria using cadastre information, LiDAR and image matching. Int. Arch. Photogramm. Remote Sens. Spatial Inform. Sci. XLI-B4, 747–754.

Schwab, B., Kolbe, T.H., 2019. Requirement analysis of 3D road space models for automated driving. ISPRS Ann. Photogramm. Remote Sens. Spatial Inform. Sci. IV-4/W8, 99–106.

Special Interest Group 3D, 2020. Modeling Guide for 3D Objects - Part 2: Modeling of Buildings (LoD1, LoD2, LoD3) - SIG3D Quality Wiki EN. URL: https://en.wiki.quality.sig3d.org/index.php?title=Modeling_Guide_for_3D_Objects_-_Part_2:_Modeling_of_Buildings_(LoD1,_LoD2,_LoD3) (accessed: 2021-10-30).

Stritih, A., Rabe, S.-E., Robaina, O., Grêt-Regamey, A., Celio, E., 2020. An online platform for spatial and iterative modelling with bayesian networks. Environ. Model. Softw. 127, 104658.

Suveg, I., Vosselman, G., 2000. 3D reconstruction of building models. ISPRS Arch. Photogramm. Remote Sens. Spatial Inform. Sci. XXXIII, 538–545.

TUM Geoinformatics, 2022. TUM Streetspace and Buildings textured with TrueDOP20, TUM Campus, Theresienstr., Munich, Germany. 3D Buildings data layer. URL: https://wiki.tum.de/display/gisproject/Online+Demo+Collection (accessed: 2022-01-25).

Tuttas, S., Stilla, U., 2013. Reconstruction of façades in point clouds from multi aspect oblique ALS. ISPRS Ann. Photogramm. Remote Sens. Spatial Inf. Sci. II-3/W3, 91–96.

Tuttas, S., Stilla, U., Braun, A., Borrmann, A., 2015. Validation of BIM components by photogrammetric point clouds for construction site monitoring. ISPRS Ann. Photogramm. Remote Sens. Spatial Inf. Sci. II-3/W4, 231–237.

U.S. Department of Transportation, 2014. Mitigation strategies for design exceptions: Vertical clearance. US Department of Transportation Federal Highway Administration. URL: https://safety.fhwa.dot.gov/geometric/pubs/mitigationstrategies/chapter3/3_verticalclearance.cfm (accessed: 2021-03-26).

Willenborg, B., Pültz, M., Kolbe, T.H., 2018a. Integration of semantic 3D city models and 3D mesh models for accuracy improvements of solar potential analyses. ISPRS Arch. Photogramm. Remote Sens. Spatial Inf. Sci. XLII-4/W10, 223–230.

Willenborg, B., Sindram, M., Kolbe, T.H., 2018b. Applications of 3D city models for a better understanding of the built environment. In: Behnisch, M., Meinel, G. (Eds.), Trends in Spatial Analysis and Modelling: Decision-Support and Planning Strategies. Springer International Publishing, Cham, Germany, pp. 167–191.

Wong, K., Gu, Y., Kamijo, S., 2020. Mapping for autonomous driving: Opportunities and challenges. IEEE Intell. Transp. Syst. Mag. 13, 91–106.

Wysocki, O., 2022a. Github repository: OloOcki/conflict-mls-citygml-detection: Release v1.0. doi: 10.5281/zenodo.6054788. URL: doi: 10.5281/zenodo.6054788 (accessed: 2022-02-12).

Wysocki, O., 2022b. Underpasses around the world. URL: https://wiki.tum.de/display/vandersar/Underpasses+around+the+world (accessed: 2022-05-09).

Wysocki, O., Hoegner, L., Stilla, U., 2022. TUM-FAÇADE: Reviewing and enriching point cloud benchmarks for façade segmentation. Int. Arch. Photogramm. Remote Sens. Spatial Inform. Sci. XLVI-2/W1-2022, 529–536.

Wysocki, O., Schwab, B., Hoegner, L., Kolbe, T., Stilla, U., 2021a. Plastic surgery for 3D city models: A pipeline for automatic geometry refinement and semantic enrichment. ISPRS Ann. Photogramm. Remote Sens. Spatial Inform. Sci. V-4, 17–24.

Wysocki, O., Xu, Y., Stilla, U., 2021b. Unlocking point cloud potential: Fusing MLS point clouds with semantic 3D building models while considering uncertainty. ISPRS Ann. Photogramm. Remote Sens. Spatial Inf. Sci. VIII-4/W2, 45–52.

Wysocki, O., Zhang, J., Stilla, U., 2021c. TUM-FAÇADE: a database of annotated façade point clouds. doi: 10.14459/2021mp1636761.001. URL: https://mediatum.ub.tum.de/1636761 (accessed: 2021-12-01).

Wyvill, G., Kunii, T.L., 1985. A functional model for constructive solid geometry. Visual Comput. 1, 3–14.

Xu, Y., Stilla, U., 2021. Towards building and civil infrastructure reconstruction from point clouds: A review on data and key techniques. IEEE J. Sel. Top. Appl. Earth Observ. Remote Sens. 14, 2857–2885.

Zeibak, R., Filin, S., 2008. Change detection via terrestrial laser scanning. ISPRS Arch. Photogramm. Remote Sens. Spatial Inf. Sci. Inf. Sci. XXXVI-3/W52, 430–435.

Zhu, J., Gehrung, J., Huang, R., Borgmann, B., Sun, Z., Hoegner, L., Hebel, M., Xu, Y., Stilla, U., 2020. TUM-MLS-2016: An annotated mobile lidar dataset of the TUM city campus for semantic point cloud interpretation in urban areas. Remote Sens. 12, 1875.

Zhu, W., Hua, Y., & Dogan, T. (2019). Evaluating street quality for walkability from 3d models. In IOP Conference Series: Earth and Environmental Science (p. 012025). IOP Publishing volume 294.